





**Real-time parameter estimation for two-qubit systems based on hybrid control**Yue Tian <sup>1</sup>, Xiujuan Lu <sup>2</sup>, Sen Kuang <sup>1,\*</sup> and Daoyi Dong <sup>3</sup><sup>1</sup>*Department of Automation, University of Science and Technology of China, Hefei 230027, China*<sup>2</sup>*Department of Mechanical Engineering, University of Hong Kong, Hong Kong 999077, China*<sup>3</sup>*School of Engineering, Australian National University, Canberra ACT 2601, Australia*

(Received 9 January 2024; accepted 5 June 2024; published 20 June 2024)

In this paper, we consider the real-time parameter estimation problem for a ZZ-coupled system composed of two qubits in the presence of spontaneous emission. To enhance the estimation precision of the coupling coefficient, we first propose two different control strategies, where the first one is feedback control based on quantum-jump detection, and the second one is hybrid control combining Markovian feedback and Hamiltonian control. The simulation results show that compared with free evolution, both control strategies can improve parameter precision and extend system coherence time. Then, on the basis of the two control strategies, we propose a practical single-parameter quantum recovery protocol, which includes the preparation of an optimal initial probe state, the active control and optimization of a system evolution process, the design of an adaptive measurement scheme, and the parameter estimation algorithm based on Bayesian estimation theory. In particular, by employing a batch-style adaptive measurement scheme, the parameter recovery is conducted and the effectiveness of the two control strategies is verified.

DOI: [10.1103/PhysRevA.109.062222](https://doi.org/10.1103/PhysRevA.109.062222)**I. INTRODUCTION**

Quantum metrology is a scientific discipline that explores the measurement, estimation, and control of quantum states and quantum systems. As an important subfield, quantum parameter estimation aims at obtaining parameter information by preparing the initial probe state, controlling the evolution process, and seeking the optimal measurements. It primarily focuses on how to leverage the nonclassical properties of quantum systems (such as entanglement, superposition, and coherence) to surpass the traditional shot-noise limit (SNL) and even achieve the Heisenberg limit (HL) [1–3]. Due to its crucial role in various fields, such as quantum gate calibration in quantum computing [4,5], channel estimation in quantum communication [6,7], and precision measurement in quantum sensing [8–10], quantum parameter estimation has become one of the research fields that attracts much attention in the quantum information science community.

Up to the current development of quantum metrology, the majority of literature on parameter estimation focuses on single-qubit systems [11–17], which are relatively simple and easy to control. Remarkable achievements include high-precision measurements of multiplicative Hamiltonian parameters and dissipative coefficients under nonunitary evolution [3,12]. However, there is a paucity of literature addressing the parameters between multiple qubit systems. In fact, in the fields of quantum communication and quantum computing, the interaction term between two qubits is one of the key resources to generate and control quantum entanglement [18,19]. Furthermore, understanding the nature of

system interactions also contributes to identifying the sources of noise, thereby facilitating improved noise suppression. That is to say, it is crucial to accurately estimate the interaction term for quantum technology applications [20,21].

In the field of quantum metrology, active control plays a fundamental role in enhancing parameter estimation performance [22–25]. In terms of open-loop control, Hamiltonian control based on numerical optimization has been demonstrated to effectively improve the estimation performance of qubit systems, including gradient ascent pulse engineering (GRAPE) [14,22], Krotov's method [11], deep deterministic policy gradients (DDPG) [25,26], and asynchronous advantage actor-critic (A3C) [27]. In terms of closed-loop control, two commonly used and easily implementable techniques are quantum-jump feedback control and homodyne-mediated feedback control [11–13,28,29]. These methods use real-time measurements to reduce the disturbance caused by the unpredictable environmental interference. Currently, closed-loop feedback control has been utilized for the generation of entangled steady states [30], control of entropy uncertainty [31], and manipulation of quantum discord dynamics in two-atom systems [32]. In this paper, we consider the estimation problem of the coupling coefficient in the presence of spontaneous emission noise in a two-qubit system. We first propose a local feedback control strategy based on quantum-jump detection, which only needs to act on one qubit to achieve precision enhancement. Then, a hybrid control strategy for the two-qubit system is proposed, which not only retains the compensation function of feedback control against stochastic disturbances but also incorporates the flexibility of Hamiltonian control.

To recover the information of system parameters to the maximum extent, various quantum estimation algorithms have been developed, including Bayesian mean estimation (BME)

\*Contact author: [skuang@ustc.edu.cn](mailto:skuang@ustc.edu.cn)

[33,34], maximum likelihood estimation (MLE) [35], and least squares estimation (LSQ) [36,37]. However, the existing literature often treats the control and optimization process and the parameter recovery step separately, resulting in a loose connection between them. In this paper, we propose a practical single-parameter quantum recovery protocol to achieve high-precision estimation of the coupling coefficient  $g$  of the ZZ coupling between two qubits. The proposed protocol demonstrates a complete parameter estimation process. First, by calculating the pure state of maximizing quantum Fisher information (QFI) without control and noise, an optimal initial probe state is obtained. Second, we propose two control strategies including local feedback control and hybrid control to improve parameter estimation precision and extend system coherence time. Finally, we design an adaptive measurement scheme and a parameter estimation algorithm based on Bayesian estimation theory, and apply the two control strategies to the parameter recovery process and achieve the high-precision estimation of the unknown parameter  $g$ .

This paper is organized as follows. In Sec. II, we introduce the Fisher information for parameter estimation and provide a brief description of the physical model under consideration. In Sec. III, the impact of feedback control on parameter estimation precision under different detection efficiencies is investigated, and the hybrid control strategy is designed to further enhance parameter estimation performance. In Sec. IV, we devise an adaptive measurement scheme and propose a batch single-parameter quantum recovery protocol based on Bayesian estimation theory. The work is summarized in Sec. V.

## II. BACKGROUND KNOWLEDGE ON QUANTUM PARAMETER ESTIMATION

In this section, we introduce several common precision evaluation criteria, and show how to obtain a set of optimal measurements. Then, the evolution model of the two-qubit system under consideration is presented, and the feedback control model is further derived.

### A. Fisher information

In the field of quantum sensing, the core task of parameter estimation is to obtain unknown system parameters by manipulating quantum states and employing appropriate measurement operations. For an open quantum system, let  $\theta$  be a single unknown parameter to be estimated, which may be a physical quantity such as coupling coefficient  $g$  [21], magnetic field strength  $\omega$  [11], or dissipation rate  $\gamma$  [12]. To begin the estimation process, an initial probe state  $\rho_0$  is prepared and evolves in a quantum channel  $\xi_\theta$ . By applying appropriate measurement operators  $\{M_y\}$  ( $\sum_y M_y = I$ , where  $I$  is the identity matrix) to the evolving state, the probability density function of measurement results  $p_\theta(y)$  is obtained. Subsequently, with the assistance of suitable estimation algorithms, the unknown parameters can be effectively estimated [38]. According to the Cramér-Rao bound [12], the lower bound of the variance  $\text{Var}(\hat{\theta})$  of the unbiased estimator  $\hat{\theta}$  satisfies

$$\text{Var}(\hat{\theta}) \geq \frac{1}{n\mathcal{I}_\theta} \geq \frac{1}{n\mathcal{F}_\theta}, \quad (1)$$

where  $n$  is the number of repeated experiments,  $\mathcal{I}_\theta$  stands for the classical Fisher information (CFI), and  $\mathcal{F}_\theta$  represents the QFI [34]. From Eq. (1), it is clear that larger Fisher information implies a smaller variance limit for the estimator, thereby enabling a higher estimation precision.

In classical parameter estimation theory, CFI is an important statistical concept, which is used to describe the distinguishability of probability space and thus quantify the limit of estimation precision [22]. For a set of probability distributions  $p_\theta(y) = \text{Tr}(\rho_\theta M_y)$  of discrete measurement outcomes,  $\mathcal{I}_\theta$  is defined as [14]

$$\mathcal{I}_\theta = \sum_y p_\theta(y) \left[ \frac{d \ln p_\theta(y)}{d\theta} \right]^2, \quad (2)$$

where  $\ln(\cdot)$  represents the natural logarithm, and  $\text{Tr}(\cdot)$  is the trace operation. CFI is fundamentally a function of measurements. To achieve higher estimation precision, the choice of measurement operators is crucial. By using the Cauchy-Schwartz inequality [39], it can be proved that CFI is equivalent to QFI under the action of the optimal measurement operators, i.e.,  $\max_{\{M_y\}} \mathcal{I}_\theta(\rho_\theta, \{M_y\}) = \mathcal{F}_\theta$  [40].

As a basic quantity in quantum physics, QFI has widespread applications in quantum metrology [22], quantum phase transitions [40], and other fields.  $\mathcal{F}_\theta$  is defined as [11]

$$\mathcal{F}_\theta = \text{Tr}[(L_s^\theta)^2 \rho_\theta]. \quad (3)$$

Here,  $L_s^\theta$  represents the symmetric logarithmic derivative (SLD) operator of  $\theta$ , which is similar to the logarithmic derivative (LD) in classical statistics. SLD can capture the response information of quantum states to small changes in parameters, which is also an important tool to determine the optimal measurement and plays a key role in quantum parameter estimation [41]. SLD can be defined as

$$\partial_\theta \rho_\theta = \frac{1}{2} (L_s^\theta \rho_\theta + \rho_\theta L_s^\theta), \quad (4)$$

where  $\partial_\theta \rho_\theta$  is the partial derivative of the quantum state  $\rho_\theta$  with respect to  $\theta$ .

We conduct spectral decomposition on the density matrix  $\rho_\theta$  and have  $\rho_\theta = \sum_i \lambda_i |\lambda_i\rangle \langle \lambda_i|$ . Substituting it into Eq. (4) gives  $\langle \lambda_i | \partial_\theta \rho_\theta | \lambda_j \rangle = \frac{1}{2} (\lambda_i + \lambda_j) \langle \lambda_i | L_s^\theta | \lambda_j \rangle$ . Further solving for  $L_s^\theta$  yields

$$L_s^\theta = \sum_{i,j, \lambda_i + \lambda_j > 0} 2 \frac{\langle \lambda_i | \partial_\theta \rho_\theta | \lambda_j \rangle}{\lambda_i + \lambda_j} |\lambda_i\rangle \langle \lambda_j|. \quad (5)$$

Since the SLD operator is a Hermitian operator, it can be diagonalized, whose eigenvectors correspond to a set of orthogonal normalized bases. For single-parameter estimation problems, the eigenvectors of SLD can be used to construct a set of optimal measurement bases [40]. Here, the set of eigenvectors of  $L_s^\theta$  is denoted as  $\{|e_i\rangle\}$ , and the corresponding projectors are considered as a set of positive-operator valued measures (POVM), denoted as  $\{E_i\} = \{|e_i\rangle \langle e_i|\}$ . Then, the probability of the  $i$ th measurement outcome is  $\langle e_i | \rho_\theta | e_i \rangle$ . With  $L_s^\theta = \sum_i e_i |e_i\rangle \langle e_i|$  and Eq. (4), we can obtain  $\langle e_i | \partial_\theta \rho_\theta | e_i \rangle = e_i \langle e_i | \rho_\theta | e_i \rangle$ . Substituting it into Eqs. (2) and (3),

we have

$$\begin{aligned} \mathcal{I}_\theta &\leq \sum_i \frac{\langle e_i | \partial_\theta \rho_\theta | e_i \rangle^2}{\langle e_i | \rho_\theta | e_i \rangle} = \sum_i e_i^2 \langle e_i | \rho_\theta | e_i \rangle \\ &= \text{Tr} \left[ \sum_i e_i^2 \rho_\theta | e_i \rangle \langle e_i | \right] = \mathcal{F}_\theta. \end{aligned} \quad (6)$$

From Eq. (6), it can be proved that the measurements under this set of projection measurements  $\{E_i\}$  maximize the parameter estimation precision [40]. It should be noted that, in most cases,  $E_i$  depends on the true value of  $\theta$ . Considering the limitations of prior knowledge in actual situations, it is usually necessary to find optimal measurements in an adaptive way.

This paper focuses on enhancing the single-parameter estimation precision. In this case, there always exists a specific set of optimal measurements that can achieve the precision defined by QFI [40], as expressed in Eq. (3). Therefore, QFI is chosen as the objective function for the optimization process. According to Eqs. (3) and (4), it is clear that the maximization of QFI depends on the evolving state  $\rho_\theta$  and its sensitivity to the parameter. This dependency involves factors such as the initial state  $\rho_0$ , degree of dissipation, and control Hamiltonian [40].

### B. Physical model

Let us consider a ZZ-coupled system composed of two spin-1/2 subsystems, with energy levels  $|e^{(k)}\rangle$  and  $|f^{(k)}\rangle$  for the  $k$ th qubit ( $k = 1, 2$ ). The model of this system has widespread applications in strong-field regimes [22]. In the absence of control, the system dynamics can be described by the Lindblad master equation as

$$\dot{\rho} = \mathcal{L}(\rho) = -\frac{i}{\hbar}[H, \rho] + \mathcal{L}_{\mathcal{D}}(\rho), \quad (7)$$

where  $\mathcal{L}$  represents the superoperator of the system evolution, and  $\mathcal{L}_{\mathcal{D}}(\rho)$  describes the decoherence caused by the environment.  $\hbar$  is the reduced Planck constant, taken as  $\hbar = 1$  in this paper.  $H = H_0 + H_c$ , where  $H_0$  is the free Hamiltonian and  $H_c$  is the control Hamiltonian. For the ZZ-coupled system, the free Hamiltonian can be written as [21]

$$H_0 = \omega_1 \sigma_z^{(1)} + \omega_2 \sigma_z^{(2)} + g \sigma_z^{(1)} \sigma_z^{(2)}, \quad (8)$$

where  $\sigma_z^{(1)} = \sigma_z \otimes I$ ,  $\sigma_z^{(2)} = I \otimes \sigma_z$ , and  $\sigma_z = |e\rangle\langle e| - |f\rangle\langle f|$ .  $\omega_1$  and  $\omega_2$  represent the local frequencies of the two qubits, respectively.  $g$  is the coupling coefficient of the ZZ coupling between the two subsystems, which is the parameter to be estimated. We assume that  $g$  has a true value of  $g^*$ . In

the case of local spontaneous emission for each qubit, the dissipative term  $\mathcal{L}_{\mathcal{D}}(\rho)$  is described as

$$\mathcal{L}_{\mathcal{D}}(\rho) = \sum_{k=1,2} \gamma_k \left[ \sigma_-^{(k)} \rho \sigma_+^{(k)} - \frac{1}{2} (\sigma_+^{(k)} \sigma_-^{(k)} \rho + \rho \sigma_+^{(k)} \sigma_-^{(k)}) \right], \quad (9)$$

where  $\gamma_k$  represents the dissipation rate of the  $k$ th qubit. We assume that the dissipative rates for both qubits are the same, i.e.,  $\gamma_1 = \gamma_2 = \gamma$  ( $\gamma \geq 0$ ).  $\sigma_-^{(k)} = |f^{(k)}\rangle\langle e^{(k)}|$  and  $\sigma_+^{(k)} = |e^{(k)}\rangle\langle f^{(k)}|$  serve as the lowering and raising operators of the  $k$ th qubit.

Note that the existence of the dissipative term leads to the loss of information in the evolution of the quantum state, and thereby a reduction in the accuracy of parameter estimation. Feedback control can be used to address this challenge [40]. Before introducing the system model with feedback control, we discuss the relationship between open quantum dynamics and quantum measurement. By discretizing the stochastic master equation (7) and comparing with the general form of quantum measurement  $\rho(t+dt) = \sum_{k=0,1} \Omega_k(dt) \rho(t) \Omega_k^\dagger(dt)$  [42], one can obtain

$$\begin{cases} \Omega_1(dt) = \sqrt{\gamma dt} \sigma_- \\ \Omega_0(dt) = I - \left( iH + \frac{\gamma}{2} \sigma_+ \sigma_- \right) dt \end{cases}, \quad (10)$$

where  $\Omega_1(dt)$  and  $\Omega_0(dt)$  are measurement operators. To be specific, if a photon is detected (as the result of energy level transition), the measurement outcome is recorded as 1, and the corresponding transition process is represented by the operator  $\Omega_1(dt)$ . Conversely, if no transition event is detected, the measurement outcome is recorded as 0, and the corresponding process is represented by the operator  $\Omega_0(dt)$ . For more details, please refer to Ref. [11].

Now, we consider the system model in the presence of feedback control. The system (7) is continuously monitored through a photon detector  $D$ . When the detector  $D$  detects a photon, a unitary evolution, denoted by  $U_{fb}$ , is triggered as a feedback to the spin to correct the dynamics of the system. No control is applied at other times, and  $U_{fb}$  is precisely the feedback control law that needs to be designed subsequently. At time  $t+dt$ , the density matrix with feedback control can be represented as

$$\begin{aligned} \rho(t+dt) &= U_{fb} \Omega_1(dt) \rho(t) \Omega_1^\dagger(dt) U_{fb}^\dagger \\ &\quad + \Omega_0(dt) \rho(t) \Omega_0^\dagger(dt). \end{aligned} \quad (11)$$

Substituting Eq. (10) into Eq. (11), we have Eq. (12),

$$\rho(t+dt) = \rho(t) + \left\{ -i[H, \rho(t)] + \sum_{k=1,2} \gamma_k \left[ U_{fb} \sigma_-^{(k)} \rho(t) \sigma_+^{(k)} U_{fb}^\dagger - \frac{1}{2} (\sigma_+^{(k)} \sigma_-^{(k)} \rho(t) + \rho(t) \sigma_+^{(k)} \sigma_-^{(k)}) \right] \right\} dt + O(dt^2) \quad (12)$$

$$\dot{\rho} = -i[H, \rho] + \sum_{k=1,2} \gamma_k \left[ U_{fb} \sigma_-^{(k)} \rho \sigma_+^{(k)} U_{fb}^\dagger - \frac{1}{2} (\sigma_+^{(k)} \sigma_-^{(k)} \rho + \rho \sigma_+^{(k)} \sigma_-^{(k)}) \right] \quad (13)$$

When  $dt$  is small enough, the second-order infinitesimal term  $O(dt^2)$  can be ignored, and thus the dynamics under

feedback control can be described by Eq. (13). Equation (13) is an ideal feedback model where the detection efficiency is

not considered. We will provide a more realistic situation with the detection efficiency in Sec. III. To preserve the Markovian nature of the system, the feedback control must take effect within a short time after the detection event is triggered.

### III. ENHANCING QUANTUM PARAMETER ESTIMATION PRECISION

It is well known that the quantum parameter estimation mainly includes four steps: (1) preparation of the initial probe state, (2) parametrization, (3) measurement, and (4) parameter recovery [25]. In this section, we consider the first two steps. Two control strategies are proposed to improve parameter estimation precision.

For the preparation of the initial state  $|\psi_{\text{opt}}(0)\rangle$ , the objective is to maximize the sensitivity to small variations in the parameter to be estimated. Since the system (7) can achieve the highest Hamiltonian parameter estimation precision only under the free evolution and in the absence of noise [22], the optimal probe state can be chosen as a pure state in this case. Let the probe state at time  $t = 0$  be  $|\psi(0)\rangle = a|00\rangle + b|01\rangle + c|10\rangle + d|11\rangle$ , and the quantum state at time  $T$  be  $|\psi(T)\rangle$ . The corresponding QFI can be obtained as [22]

$$\mathcal{F}_g = 4\text{Re}[\langle \partial_g \psi(T) | \partial_g \psi(T) \rangle - \langle \partial_g \psi(T) | \psi(T) \rangle \langle \psi(T) | \partial_g \psi(T) \rangle], \quad (14)$$

where  $\text{Re}[\cdot]$  represents the real part.  $|\partial_g \psi(T)\rangle$  is the partial derivative of the quantum state  $|\psi(T)\rangle$  with respect to the coupling coefficient  $g$ .

Note in our context, the parameter  $\theta$  in Eq. (3) is replaced by the coupling coefficient  $g$ . Substituting the system state  $|\psi(T)\rangle = e^{-i(w_1\sigma_z^{(1)} + w_2\sigma_z^{(2)} + g\sigma_z^{(1)}\sigma_z^{(2)})T} |\psi(0)\rangle$  at time  $T$  without control and noise into Eq. (14) gives

$$\mathcal{F}_g = 4T^2 \{1 - [\langle \psi(0) | \sigma_z^{(1)} \sigma_z^{(2)} | \psi(0) \rangle]^2\}. \quad (15)$$

To achieve the highest sensitivity, the metric  $\mathcal{F}_g$  needs to be maximized, i.e., the condition  $\langle \psi(0) | \sigma_z^{(1)} \sigma_z^{(2)} | \psi(0) \rangle = 0$  holds. Moreover, with the normalization condition of the state vector, we have

$$\begin{cases} |a|^2 - |b|^2 - |c|^2 + |d|^2 = 0 \\ |a|^2 + |b|^2 + |c|^2 + |d|^2 = 1 \end{cases} \Rightarrow \begin{cases} |a|^2 + |d|^2 = \frac{1}{2} \\ |b|^2 + |c|^2 = \frac{1}{2} \end{cases}. \quad (16)$$

Thus, we can choose an optimal probe state as

$$|\psi_{\text{opt}}(0)\rangle = \frac{1}{2}|00\rangle + \frac{1}{2}|01\rangle + \frac{1}{2}|10\rangle + \frac{1}{2}|11\rangle = |++\rangle, \quad (17)$$

where  $|+\rangle = \frac{1}{\sqrt{2}}(|0\rangle + |1\rangle)$ . In the succeeding study, this state will always be used as the initial probe state unless otherwise stated.

#### A. Without control

After preparing the initial probe state, we first analyze the estimation precision under the free evolution. For the system (7) without control, we estimate the coupling coefficient  $g$  between the qubits. Denote the density matrix of the system

at time  $t$  as

$$\rho(t) = \begin{bmatrix} \rho_{11}(t) & \rho_{12}(t) & \rho_{13}(t) & \rho_{14}(t) \\ \rho_{12}^*(t) & \rho_{22}(t) & \rho_{23}(t) & \rho_{24}(t) \\ \rho_{13}^*(t) & \rho_{23}^*(t) & \rho_{33}(t) & \rho_{34}(t) \\ \rho_{14}^*(t) & \rho_{24}^*(t) & \rho_{34}^*(t) & \rho_{44}(t) \end{bmatrix}. \quad (18)$$

With the optimal initial probe state  $|\psi_{\text{opt}}(0)\rangle$  in (17), substituting Eq. (18) into Eq. (7), we can calculate the analytical solutions for the elements of  $\rho(t)$  as

$$\begin{aligned} \rho_{11}(t) &= \frac{1}{4} \exp[-(\gamma_1 + \gamma_2)t] \\ \rho_{12}(t) &= \frac{1}{4} \exp[-(2\gamma_1 + \gamma_2)t - i(2\omega_2 + 2g)t] \\ \rho_{13}(t) &= \frac{1}{4} \exp[-(\gamma_1 + 2\gamma_2)t - i(2\omega_1 + 2g)t] \\ \rho_{14}(t) &= \frac{1}{4} \exp\left[-\frac{1}{2}(\gamma_1 + \gamma_2)t - i(2\omega_1 + 2\omega_2)t\right] \\ \rho_{22}(t) &= \frac{1}{2} \exp(-\gamma_1 t) - \frac{1}{4} \exp[-(\gamma_1 + \gamma_2)t] \\ \rho_{23}(t) &= \frac{1}{4} \exp\left[-\frac{1}{2}(\gamma_1 + \gamma_2)t - 2(\omega_1 - \omega_2)t\right] \\ \rho_{24}(t) &= \exp\left[\chi_1 \frac{2g - i\gamma_2}{2(4g - i\gamma_2)}\right] \\ &\quad + i\gamma_2 \exp\left[-\frac{1}{2}(\gamma_1 + 2\gamma_2)t + i(4g + 4\omega_1)t\right] \varrho_2 \\ \rho_{33}(t) &= \frac{1}{2} \exp(-\gamma_2 t) - \frac{1}{4} \exp[-(\gamma_1 + \gamma_2)t] \\ \rho_{34}(t) &= \exp\left[\chi_2 \frac{2g - i\gamma_1}{2(4g - i\gamma_1)}\right] \\ &\quad + i\gamma_1 \exp\left[-\frac{1}{2}(2\gamma_1 + \gamma_2)t + i(4g + 4\omega_2)t\right] \varrho_1 \\ \rho_{44}(t) &= \frac{1}{4} \exp[-(\gamma_1 + \gamma_2)t] - \frac{1}{2} \exp(-\gamma_1 t) \\ &\quad - \frac{1}{2} \exp(-\gamma_2 t) + 1, \end{aligned} \quad (19)$$

where  $\chi_k = -\frac{1}{2}\gamma_k t - i(4g - 4\omega_k)t$ ,  $\varrho_k = \frac{1}{4(4g - i\gamma_k)}$ , and  $k \in \{1, 2\}$ . Based on Eqs. (3), (18), and (19), one can obtain  $\mathcal{F}_g$ . We plot the change curves of  $\mathcal{F}_g$  with the dissipation rate  $\gamma$  and time  $t$  in Fig. 1. It can be observed from Fig. 1(a) that the increase in the dissipation rate causes a rapid deterioration of  $\mathcal{F}_g$  at the terminal time  $T = 80$ . In particular, the estimation capability almost vanishes when  $\gamma$  reaches 0.05. Hence,  $\gamma = 0.05$  is chosen as the dissipation rate in the subsequent analysis. During the evolution process in Fig. 1(b),  $\mathcal{F}_g$  gradually increases over time until it reaches a peak, and then begins to decrease. This implies that the uncertainty introduced by noise affects the parameter estimation accuracy of the system (7). Specifically, for the studied open quantum system (7), its coherence gradually becomes weak due to the influence of the environment, ultimately leading to significant decrease in the parameter estimation precision after  $t = 41.6$  for  $g^* = 0.1$  and  $t = 37.6$  for  $g^* = 0.2$ .

#### B. Feedback control

In this subsection, we examine the impact of quantum-jump feedback control on the dynamics and analyze the control performance. Under feedback control, the system is described by Eq. (13), and the final parameter estimation precision depends on the choice of feedback operator  $U_{fb}$ . Once a transition event represented by  $\sigma_-^{(k)} \rho \sigma_+^{(k)}$  is detected, the operator  $U_{fb} = \exp[iH_{fb}\delta_t]$  immediately acts on the system within an extremely short time  $\delta_t$ , where  $H_{fb}$  is a

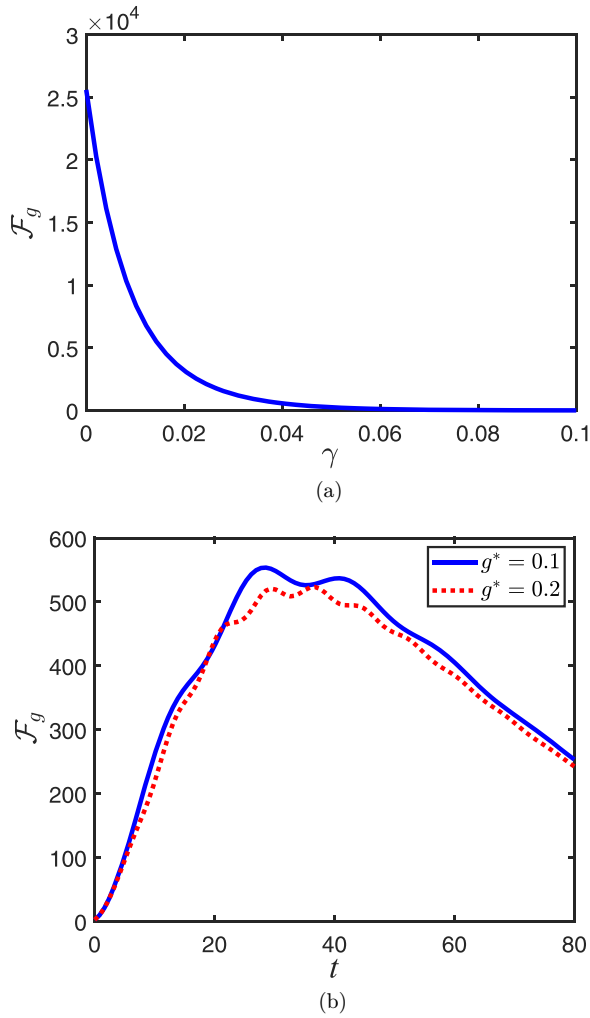


FIG. 1. (a) Without control, the change curve of  $\mathcal{F}_g$  at the terminal time  $T = 80$  with the dissipation rate  $\gamma$ , where the true value of  $g$  is set as  $g^* = 0.1$ . (b) The change curves of QFI with time  $t$  under different values of  $g^*$ , where the solid blue line and the dotted red line correspond to  $g^* = 0.1$  and  $g^* = 0.2$ , respectively. Other parameters are chosen as  $\omega_1 = \omega_2 = 1$  and  $\gamma = 0.05$ .

Hermitian operator. Under the constraint of  $U_{fb}U_{fb}^\dagger = I$ , a feedback mechanism that can break the exchange symmetry between atoms is considered, aiming to limit destructive interference. Here, we apply feedback to only one of the qubits, i.e., local feedback. The selected feedback operator  $U_{fb}$  is [30]

$$U_{fb} = e^{i\lambda\sigma_x} \otimes I, \quad (20)$$

where  $\lambda$  represents the feedback strength ( $0 \leq \lambda \leq \pi$ ).

In practice, due to non-negligible error limitations on the experimental components, the efficiency  $\eta$  of the detector  $D$  is difficult to reach 1, while the detection information directly affects the effectiveness of feedback control. Therefore, the analysis of detection efficiency is also necessary.

### 1. Perfect detection ( $\eta = 1$ )

Here, we analyze the case of perfect detection efficiency ( $\eta = 1$ ), i.e., the detector successfully detects all photons and responds accordingly. In this case, the master equation of

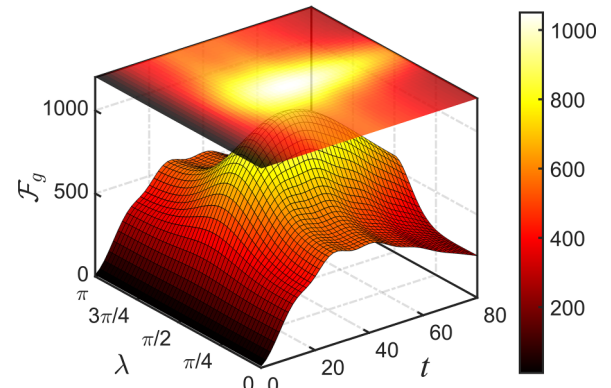


FIG. 2. The surface plot and its top view mapping of  $\mathcal{F}_g$  with respect to both time  $t$  and the feedback strength  $\lambda$  under feedback control. The true value of  $g$  is set as  $g^* = 0.1$ . Other parameters are chosen as  $\omega_1 = \omega_2 = 1$  and  $\gamma = 0.05$ .

the system is Eq. (13). The change surface of  $\mathcal{F}_g$  with time and the feedback strength  $\lambda$  is plotted in Fig. 2, where we project this surface onto a top plane for easy observation. From Fig. 2, it can be seen that the different values of the feedback strength  $\lambda$  have varying effects on the function  $\mathcal{F}_g$ .  $\lambda = 0$  corresponds to the scenario without feedback. The corresponding simulation result is consistent with that without control. As  $\lambda$  changes, the surface exhibits a hump-shaped pattern, reaching the highest point at  $\lambda = \frac{\pi}{2}$ . This indicates that the feedback operator  $U_{fb} = e^{i\frac{\pi}{2}\sigma_x} \otimes I$  can be used to enhance the parameter estimation precision. Additionally, the top plane indicates that feedback has the ability to slow down the attenuation of QFI and maintain high estimation precision even over a longer evolution time.

Next, we analyze the maximum QFI that can be achieved under different control laws. Define the peak value  $\mathcal{F}_g^{\max}$  of QFI and its improvement degree (increment)  $\Delta\mathcal{F}_g^{\max}$  as

$$\mathcal{F}_g^{\max} = \max_t[\mathcal{F}_g(t)], \quad (21)$$

$$\Delta\mathcal{F}_g^{\max} = \mathcal{F}_g^{\max}(\lambda) - \mathcal{F}_g^{\max}(0), \quad (22)$$

where  $\lambda = 0$  corresponds to the case without control.

In Fig. 3, we plot the curves of  $\mathcal{F}_g^{\max}$  and  $\Delta\mathcal{F}_g^{\max}$  under different values of  $\lambda$ . As can be seen from Fig. 3(a),  $\mathcal{F}_g^{\max}$  changes periodically with  $\lambda$ , and the period is  $\pi$ . Moreover, as  $\lambda$  approaches  $\frac{n\pi}{2}$  in the  $n$ th period, the degree of precision enhancement increases. At the peak value, the improvement reaches 90.18%, which provides a valuable reference for the selection of control strategies in the subsequent design of the parameter recovery protocol. Considering the potential limitation of insufficient prior knowledge in practical experiments, in Fig. 3(b), we illustrate the impact of feedback control on estimation precision under different values of  $g^*$ . Figure 3(b) reveals that the three different values of  $g^*$  exhibit similar precision improvement, implying the broad applicability of this optimization strategy. In addition, we also find that as  $g^*$  increases, there is an increase in the enhancement of QFI.

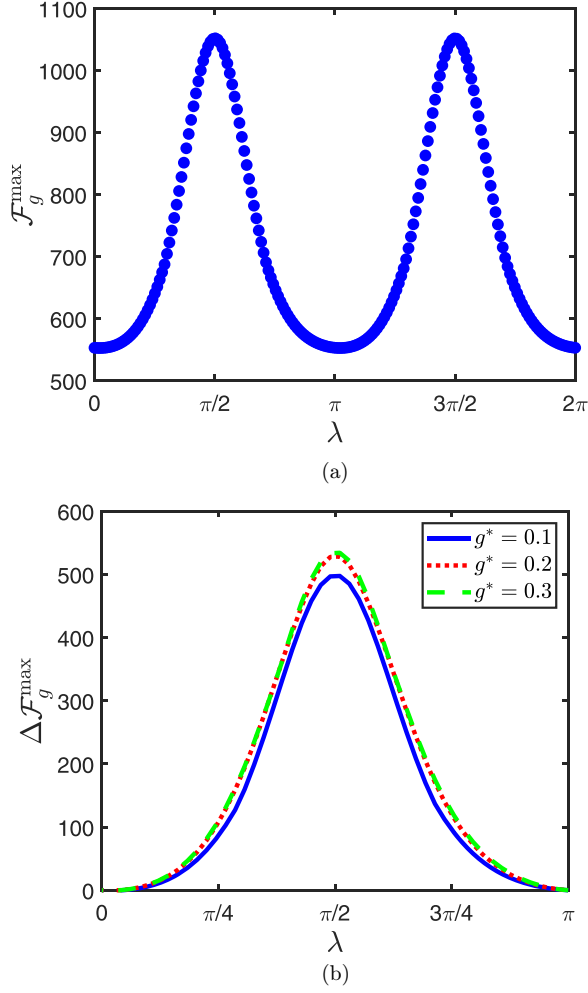


FIG. 3. (a) Under feedback control, the scatter plot of the variation of the QFI peak value  $\mathcal{F}_g^{\max}$  with the feedback strength  $\lambda$ . The true value of  $g$  is set as  $g^* = 0.1$ . (b) Under different values of  $g^*$ , the impact of feedback control on the QFI peak improvement degree  $\Delta\mathcal{F}_g^{\max}$ , where the solid blue line, the dotted red line, and the dashed green line represent  $g^* = 0.1$ ,  $g^* = 0.2$ , and  $g^* = 0.3$ , respectively. Other parameters are chosen as  $\omega_1 = \omega_2 = 1$  and  $\gamma = 0.05$ .

## 2. Imperfect detection ( $0 < \eta < 1$ )

Now, we consider another situation, where some of the emitted photons during the system transitions are not detected by the detector  $D$ .

According to the quantum measurement theory, the detection efficiency  $\eta$  can be reflected in the measurement process, i.e.,  $\rho(t+dt) = \eta U_{fb} \Omega_1(dt) \rho(t) \Omega_1^\dagger(dt) U_{fb}^\dagger + (1-\eta) \Omega_1(dt) \rho(t) \Omega_1^\dagger(dt) + \Omega_0(dt) \rho(t) \Omega_0^\dagger(dt)$  ( $0 \leq \eta \leq 1$ ). In this case, the master equation (13) is modified as

$$\begin{aligned} \dot{\rho} = & -i[H, \rho] + \eta\gamma_1 \mathcal{D}[U_{fb}\sigma_-^{(1)}]\rho \\ & + (1-\eta)\gamma_1 \mathcal{D}[\sigma_-^{(1)}]\rho + \gamma_2 \mathcal{D}[\sigma_-^{(2)}]\rho \end{aligned} \quad (23)$$

with

$$\mathcal{D}[\sigma_-^{(k)}]\rho = \sigma_-^{(k)}\rho\sigma_+^{(k)} - \frac{1}{2}(\sigma_+^{(k)}\sigma_-^{(k)}\rho + \rho\sigma_+^{(k)}\sigma_-^{(k)}). \quad (24)$$

$\eta = 0$  represents a photon detection efficiency of 0, meaning that the feedback operator is never triggered at any time. In

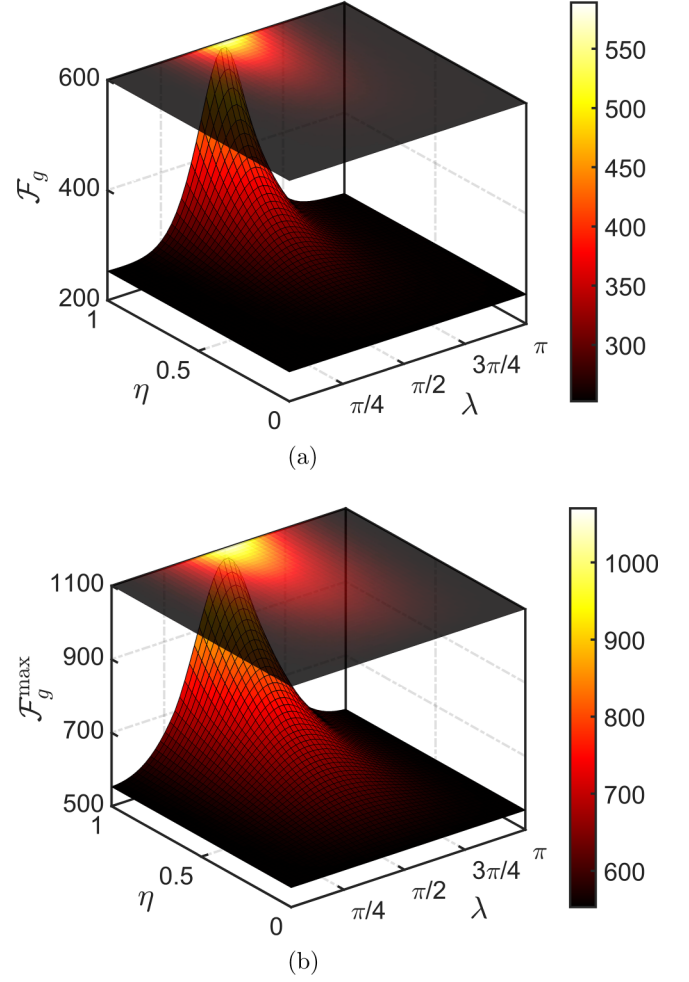


FIG. 4. (a) When  $T = 80$ , the change surface and the top mapping plane of  $\mathcal{F}_g$  with respect to the feedback strength  $\lambda$  and the detection efficiency  $\eta$ . (b) The change surface and the top mapping plane of  $\mathcal{F}_g^{\max}$  with respect to the feedback strength  $\lambda$  and the detection efficiency  $\eta$ . The true value of  $g$  is set as  $g^* = 0.1$ . Other parameters are chosen as  $\omega_1 = \omega_2 = 1$  and  $\gamma = 0.05$ .

this case, Eq. (23) is equivalent to Eq. (7).  $\eta = 1$  corresponds to the perfect detection efficiency, and in this case Eq. (23) reverts to Eq. (13), while  $0 < \eta < 1$  indicates the situation that the photon detector  $D$  only detects some photons, which is also the focus of our study in this subsection.

Similarly, we explore the optimal feedback strength under imperfect detection efficiency, where the feedback operator is of the form in Eq. (20). Figure 4(a) shows the surface of  $\mathcal{F}_g$  at  $T = 80$  with the feedback strength  $\lambda$  and the detection efficiency  $\eta$ . Furthermore, we replace the objective function  $\mathcal{F}_g$  in Fig. 4(a) with  $\mathcal{F}_g^{\max}$  represented by Eq. (21), and the result is shown in Fig. 4(b). By observing Figs. 4(a) and 4(b), it is clear that the estimation precision under any detection efficiency reaches its peak at  $\lambda = \frac{\pi}{2}$ . Thus, we obtain the optimal feedback operator as  $U_{fb} = e^{i\frac{\pi}{2}\sigma_x} \otimes I$ , which is the same as that under perfect detection efficiency.

Then, Fig. 5(a) shows how the QFI value  $\mathcal{F}_g$  changes with time  $t$  and the detection efficiency  $\eta$ . Along the time axis, the objective function  $\mathcal{F}_g$  increases gradually with the increase

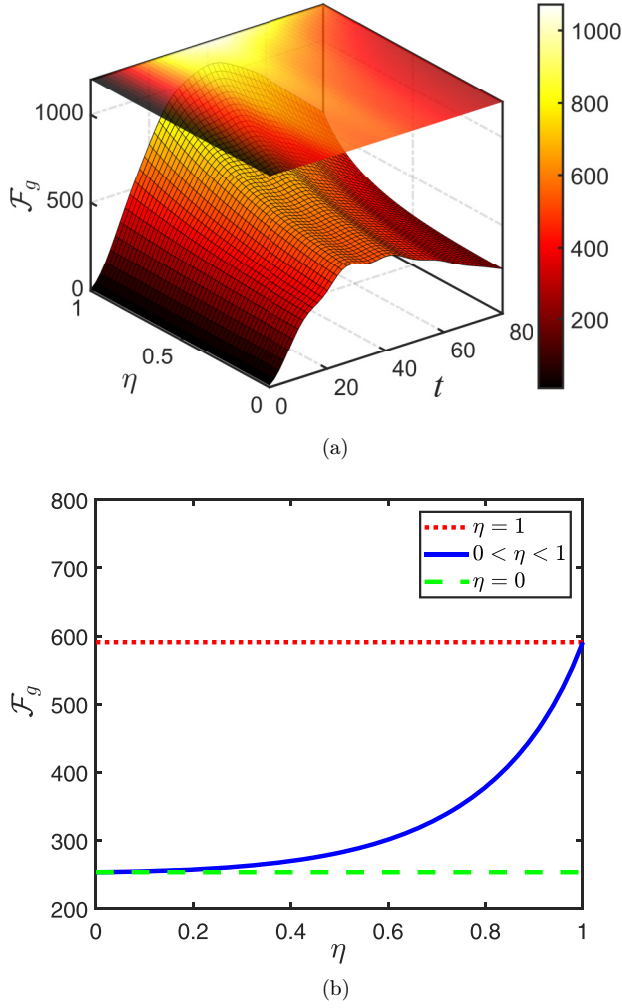


FIG. 5. (a) Under feedback control and imperfect detection, the change surface and the top mapping plane of  $\mathcal{F}_g$  with respect to time  $t$  and the detection efficiency  $\eta$ , where the feedback strength is set as  $\lambda = \frac{\pi}{2}$ . (b) When  $T = 80$ , the change curves of  $\mathcal{F}_g$  under different values of the detection efficiency  $\eta$ , where the dotted red line, the dashed green line, and the solid blue line represent  $\eta = 1$ ,  $\eta = 0$ , and  $0 < \eta < 1$ , respectively. The true value of  $g$  is set as  $g^* = 0.1$ . Other parameters are chosen as  $\omega_1 = \omega_2 = 1$  and  $\gamma = 0.05$ .

of the detection efficiency. Even with imperfect detection efficiency, the performance under feedback control is still superior to that under free evolution, which also can be verified more intuitively by Fig. 5(b). The control effect at  $T = 80$  is depicted in Fig. 5(b), showing that the detection efficiency curve of  $\eta \in (0, 1)$  lies between the perfect detection and free evolution lines. In addition, it can be seen that a higher detection efficiency leads to a faster rate of precision improvement. This indicates that feedback control significantly enhances the system's ability to suppress decoherence.

### C. Hybrid control

In the previous subsection, we analyzed the impact of quantum-jump feedback on the parameter estimation precision. The results show that the optimization strategy improves the maximum achievable QFI to some extent and

slows down the decay rate of estimation precision. However, there is still room for improvement. In this subsection, Hamiltonian control is applied to further extract the information of  $g$ . For simplicity, we assume that the perfect detection efficiency can be achieved, i.e.,  $\eta = 1$ , and controls are applied in all three directions for each qubit, i.e.,  $H_c = \sum_{k=1,2} \sum_{j=1,2,3} u_j^{(k)} \sigma_j^{(k)}$ . In this case, the system Hamiltonian can be expressed as

$$H = H_0 + H_c = \omega_1 \sigma_z^{(1)} + \omega_2 \sigma_z^{(2)} + g \sigma_z^{(1)} \sigma_z^{(2)} + \sum_{k=1,2} \vec{u}^{(k)} \cdot \vec{\sigma}^{(k)}, \quad (25)$$

where  $\vec{u}^{(k)}$  represents the control field in the three directions of the  $k$ th qubit. For the system in Eq. (13), we consider the Hamiltonian in Eq. (25) and choose  $U_{fb} = e^{i\frac{\pi}{2}\sigma_x} \otimes I$  as the feedback operator. The GRAPE algorithm [14,22] is used to find optimal control fields. In the GRAPE algorithm, the control time is divided into multiple time segments. For any control field, the control quantity on each time segment is a constant to be determined, called the control variable on this time segment associated with the control field. The partial derivative of the objective function with respect to any control variable under each control field will form a gradient component. Thus, the basic idea of the GRAPE algorithm is to first choose a set of initial control fields to drive the evolution of the quantum system, and then iteratively update the control quantity on each time segment under each control field along the gradient direction of the objective function in order to maximize the objective function. In what follows, we state the design of hybrid control with analysis.

First, the time interval  $[0, T]$  is divided into  $\mathcal{M}$  segments of length  $\delta t$  ( $\delta t = \frac{T}{\mathcal{M}}$ ). The density matrix at time  $T$  can be expressed as  $\rho(T) = \prod_{n=1}^{\mathcal{M}} \exp(\mathcal{L}_n \delta t) \rho(0)$ , where  $\mathcal{L}_n$  is the system evolution superoperator corresponding to the  $n$ th time segment, i.e.,  $\mathcal{L}_n(\rho) = -\frac{i}{\hbar} [H_0 + \sum_{k=1,2} \vec{u}^{(k)}(n) \cdot \vec{\sigma}^{(k)}, \rho] + \mathcal{L}_{\mathcal{D}}(\rho)$ . According to Eq. (3), we calculate the gradient of the objective function at time  $T$  and have

$$\frac{\partial \mathcal{F}_g(T)}{\partial u_j^{(k)}(m)} = \text{Tr} \left( \frac{\partial \mathcal{N}_m}{\partial u_j^{(k)}(m)} \rho(m \delta t) \right) + \text{Tr} \left( \mathcal{N}_m \frac{\partial \rho(m \delta t)}{\partial u_j^{(k)}(m)} \right), \quad (26)$$

where  $u_j^{(k)}(m)$  is the control variable on the  $m$ th time segment, and  $\mathcal{N}_m = \prod_{n=m+1}^{\mathcal{M}} \exp(\mathcal{L}_n \delta t) [L_s^0(T)]^2$ . Then, the control variable is updated according to the gradient information as

$$u_j^{(k)}(m) \rightarrow u_j^{(k)}(m) + \epsilon \frac{\partial \mathcal{F}_g(T)}{\partial u_j^{(k)}(m)}, \quad (27)$$

where  $\epsilon$  is the learning rate. We set the total time as  $T = 80$ , the number of time segments as  $\mathcal{M} = 100$ , and the learning rate as  $\epsilon = 0.01$ . Figure 6(a) shows how  $u_j^{(k)}$  changes with time  $t$  in six directions when the control amplitude is unconstrained. Considering some physical and technical constraints, we may need to limit the control amplitude within a certain range. From Fig. 6(a), we can see that the optimal control amplitudes in different directions differ by more than five times. In addition, during most of the time, the control values are within the range of  $\pm 0.2$ . This indicates that the control amplitude of the hybrid control strategy can be limited to

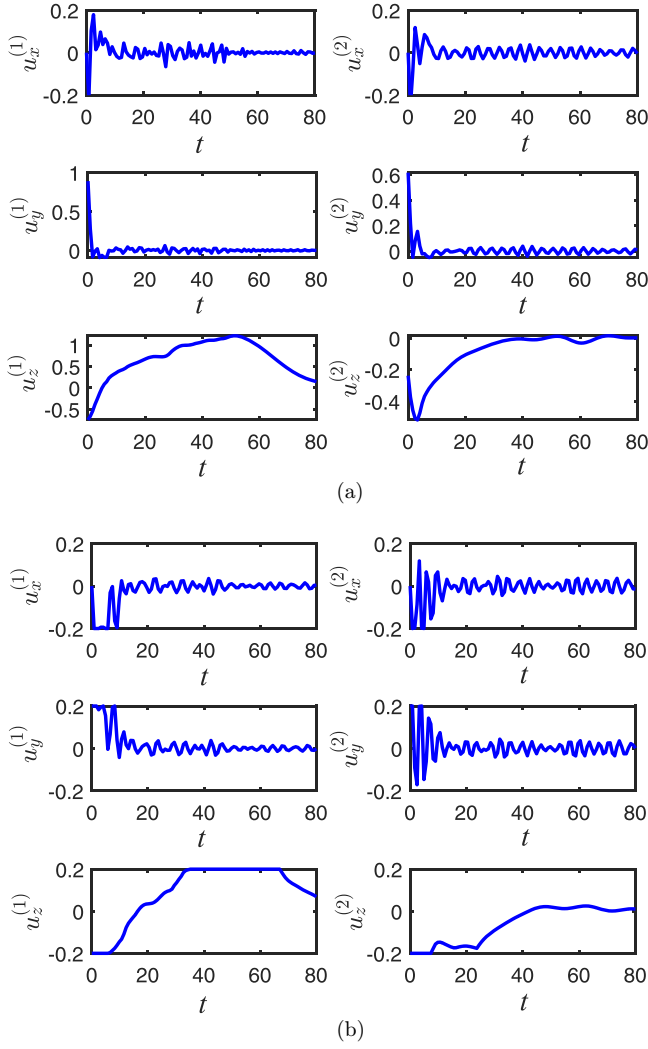


FIG. 6. (a) The optimal control law under hybrid control when there is no constraint on the control amplitude. (b) The final optimal control law when the control amplitude is constrained within  $[-0.2, 0.2]$ . In each graph, the first (second) vertical column represents the local controls applied to the first (second) qubit in three directions. Other parameters are chosen as  $g^* = 0.1$ ,  $\omega_1 = \omega_2 = 1$ , and  $\gamma = 0.05$ .

$[-0.2, 0.2]$ . The result under this control amplitude restriction is shown in Fig. 6(b).

Next, we discuss the dependence of the hybrid control strategy on the initial probe state. We choose three typical quantum states for comparison:  $|++\rangle$ ,  $|\Phi^{(+)}\rangle = (|00\rangle + |11\rangle)/\sqrt{2}$ , and  $|\Psi^{(+)}\rangle = (|01\rangle + |10\rangle)/\sqrt{2}$ . The QFI values  $\mathcal{F}_g$  under these three probe states are plotted in Fig. 7(a), which shows a similar upward trend and meanwhile implies that the hybrid control strategy can quickly adjust the initial state to the state sensitive to the unknown parameter and thereby has a high degree of freedom in the selection of the initial probe state, not limited to a specific quantum state. In addition, we also plot the change curves of  $\mathcal{F}_g$  under different  $g^*$  in Fig. 7(b). It can be seen from Fig. 7(b) that the QFIs under the three scenarios have been greatly improved with the increase of evolution time, which reflects good robustness of

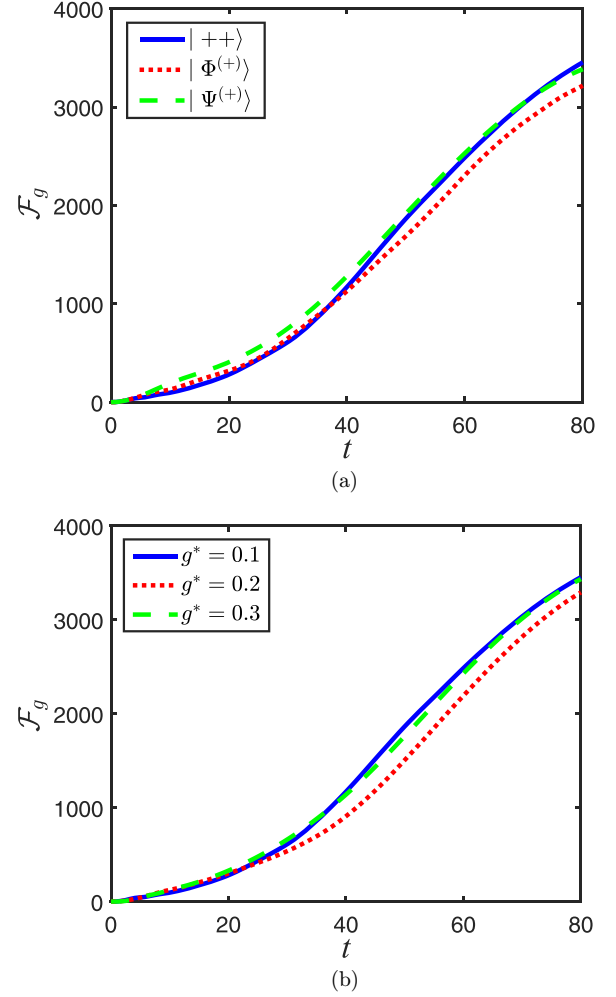


FIG. 7. (a) Under the hybrid control strategy, the influence of different initial probe states on the estimation precision of the unknown parameter, where the solid blue line, the dotted red line, and the dashed green line represent  $|++\rangle$ ,  $|\Phi^{(+)}\rangle$ , and  $|\Psi^{(+)}\rangle$ , respectively. (b) When the parameter to be estimated takes different true values, the curves of  $\mathcal{F}_g$  with respect to time  $t$ , where the solid blue line, the dotted red line, and the dashed green line represent  $g^* = 0.1$ ,  $g^* = 0.2$ , and  $g^* = 0.3$ , respectively. Other parameters are chosen as  $\omega_1 = \omega_2 = 1$  and  $\gamma = 0.05$ .

the algorithm. At the same time, it indicates that the hybrid control strategy has a low dependence on prior knowledge and is more suitable for practical scenarios.

Finally, to compare with the traditional GRAPE algorithm, we plot the curves of  $\mathcal{F}_g$  under the hybrid control strategy and the GRAPE algorithm during the iteration process in Fig. 8(a). Due to the correction effect of feedback control in the early stage, the hybrid strategy shows superior performance. After the 67th iteration, the performance is much higher than the traditional GRAPE algorithm, which once again verifies the significance of feedback control. Subsequently, both curves fluctuate around their respective stable values. Note that during the iteration process, the two curves do not always exhibit the upward trend. This is due to the nonconcave nature of the objective function, which can lead the GRAPE algorithm to get stuck in local optimum while searching for



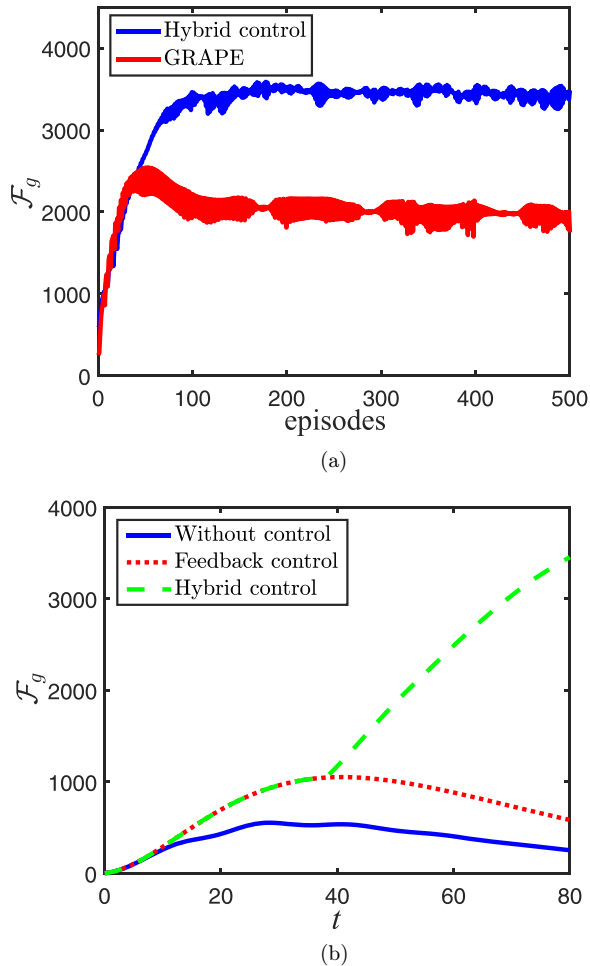


FIG. 8. (a) After 500 iterations, comparison of improvement in estimation precision between the hybrid control strategy and the GRAPE algorithm. The blue (upper) line represents the case where feedback control and additional Hamiltonian control are simultaneously applied to the system, and the red (lower) line stands for the case where only the GRAPE algorithm is applied to Hamiltonian control. (b) The change curves of  $\mathcal{F}_g$  with respect to time  $t$  for the three scenarios, where the solid blue line, the dotted red line, and the dashed green line represent no control, only feedback control, and hybrid control, respectively. Other parameters are chosen as  $g^* = 0.1$ ,  $\omega_1 = \omega_2 = 1$ , and  $\gamma = 0.05$ .

control pulses. Figure 8(b) intuitively shows the curves of  $\mathcal{F}_g$  under three different cases: no control, feedback control, and hybrid control. Before  $T = 40$ , additional Hamiltonian control has little impact on the precision improvement, and feedback control plays a key role. For simplicity, we choose the feedback control curve instead. As the decoherence effect gradually becomes apparent, the overall estimation precision without control shows the decreasing trend. However, appropriate feedback control can suppress such a decreasing trend. After that, the improvement effect of hybrid control on QFI gradually becomes evident, eventually reaching 6.24 times of the maximum precision value under free evolution. Even after a long evolution period, hybrid control can still maintain distinguishability between quantum trajectories under different

parameter true values, and extend the coherence time of the system.

#### IV. BAYESIAN BATCH SINGLE-PARAMETER QUANTUM RECOVERY PROTOCOL

In this section, we study the other two steps of parameter estimation, namely, measurement selection and parameter recovery. By combining these steps with the hybrid control strategy discussed in Sec. III, an adaptive Bayesian batch single-parameter quantum recovery protocol is proposed.

Before proceeding with protocol design, we first introduce the Bayesian estimation theory needed for parameter recovery. For the majority of problems that use prior knowledge to deal with uncertainty, Bayesian estimation demonstrates good performance. It can provide a complete probability distribution and a unique state estimate, and has wide applications in parameter estimation, decision analysis, and other fields [33]. In quantum parameter estimation, for the parameter  $\theta$  to be estimated, a set of specific POVMs  $\{M_y\}$  can be used to perform the same measurement operation on  $N$  copies of  $\rho(\theta)$ . This transforms the quantum estimation problem into a classical statistical probability problem. With the observation outcome  $y$  and the prior probability  $P(y|\theta)$ , the posterior probability  $P(\theta|y)$  is updated after each measurement. Generally, the Bayesian rule can be written as

$$P(\theta|y) = \frac{P(y|\theta)P(\theta)}{\int P(y|\theta)P(\theta)d\theta} \quad (28)$$

and the corresponding Bayesian estimator for  $\theta$  can be expressed as

$$\hat{\theta} = \int \theta P(\theta|y)d\theta. \quad (29)$$

In addition to the classical probability and statistical estimation rules, a quantum parameter recovery protocol also involves measurement scheme and simulation design [33], which will be discussed in the following subsections.

##### A. Adaptive measurement scheme

In Sec. III, the selection of optimal measurements was not considered. The reason is that the lower bound of the variance achievable by all physically allowable measurement operators is equal to the reciprocal of QFI. However, when it comes to a practical recovery protocol, we need to consider an actual measurement strategy, which is directly related to the extraction of quantum parameter information and significantly affects the final estimation precision. In the case of rich prior knowledge, it is possible to directly obtain better measurements that make CFI close to QFI. Here, our focus lies in the situation of limited prior knowledge, which is more frequently encountered in practical applications. For this, we propose an adaptive measurement scheme that incorporates the Bayesian estimation. In this scheme, a compromise parameter value is first chosen to find a set of approximately optimal measurement operators as the initial measurement set, and then this measurement operator set is continuously updated based on the observed data and the corresponding estimate of

the parameter. The specific measurement scheme is stated as follows.

The first step is to select an initial set of measurements with good robustness, which has high sensitivity to a large range of parameters to be estimated. Let us consider the estimation problem of the coupling coefficient  $g$  in the ZZ-coupled system. With Eq. (4), the eigenvectors of SLD under  $g^* = 0.1$  are calculated, and the corresponding projectors can be chosen as a set of measurement operators. Since the selection of the initial measurement set only needs to ensure that the corresponding parameter information can be extracted under different values of  $g^*$  and will be updated adaptively, it is not necessary to adopt the strictly optimal measurement set under a specific value of  $g^*$ . To simplify calculation, we approximate all elements of each measurement operator to their nearest integers. Thus, the resulting initial POVM set can be obtained as

$$\begin{aligned} M_0 &= \frac{1}{4} \begin{bmatrix} 1 & i & i & 1 \\ -i & 1 & 1 & -i \\ -i & 1 & 1 & -i \\ 1 & i & i & 1 \end{bmatrix} \\ M_1 &= \frac{1}{4} \begin{bmatrix} 1 & i & -i & -1 \\ -i & 1 & -1 & i \\ i & -1 & 1 & -i \\ -1 & -i & i & 1 \end{bmatrix} \\ M_2 &= \frac{1}{4} \begin{bmatrix} 1 & -i & i & -1 \\ i & 1 & -1 & -i \\ -i & -1 & 1 & i \\ -1 & i & -i & 1 \end{bmatrix} \\ M_3 &= \frac{1}{4} \begin{bmatrix} 1 & -i & -i & 1 \\ i & 1 & 1 & i \\ i & 1 & 1 & i \\ 1 & -i & -i & 1 \end{bmatrix}. \end{aligned} \quad (30)$$

The effectiveness of the initial measurement set in Eq. (30) will also be verified in the subsequent Sec. IV C, where this set of POVM exhibits a high distinguishability for different values of  $g^*$  within a large range, that is, the measurement results vary significantly. This implies that it is appropriate to select Eq. (30) as an initial measurement set under  $g^* = 0.1$ .

The second step is to adaptively update the measurement set. Based on the parameter information obtained from the early measured simulation data, a new estimate  $\hat{\theta}$  can be obtained. By solving Eq. (4), the SLD operator  $L_s^\theta$  associated with the estimate and thereby a new set of projective measurement bases can be obtained. It should be noted that the practical measurement overhead problem needs to be considered in the adaptive update process. Although the update of POVM after each measurement can achieve high-precision estimation level quickly, it significantly increases the computational cost and time overhead. To solve this problem, we can adopt a batch-style adaptive measurement scheme, i.e., (1) the initial measurement set is applied to  $R$  copies of the quantum state  $\rho_\theta(T)$ , called one batch, and  $R$  measurement outcomes are obtained through a sampling process, which will be described in Sec. IV B; (2) the parameter's probability distribution is calculated according to the  $R$  measurement outcomes, and the parameter estimate is obtained through Bayesian method; (3) the optimal measurement set under the

estimate is updated as the measurement set for the next batch, and is used to generate  $R$  new measurement outcomes; (4) the above steps (2) and (3) are repeated until  $N$  batches.

### B. Adaptive parameter recovery protocol with simulation

Combined with the aforementioned adaptive measurement rules, we illustrate the design of the batch-style adaptive single-parameter recovery protocol with the aid of simulation. We still consider the estimation problem of the coupling coefficient  $g$  in the ZZ-coupled system. The flowchart of the protocol is shown in Fig. 9. In the simulation, the parameters are set as follows. A total of 100 values of the coupling coefficient  $g$  are taken at equal intervals in  $[0, 0.2]$ , and their initial probability distribution is uniform, i.e.,  $P_0(g) = \frac{1}{100}$  for each value of  $g$ . The initial probe state is chosen as  $|++\rangle$ , and the initial measurement set follows Eq. (30). The true value of  $g$  is set as  $g^* = 0.1$ . The system evolves in the time interval  $[0, T]$  with the terminal time  $T = 80$ . We divide  $[0, T]$  into  $\mathcal{M} = 100$  equal portions and assume the photon detection efficiency  $\eta$  in feedback control to be 1 for simplicity. The evolution process is simulated in  $N = 20$  batches, each batch consisting of  $R = 100$  independent evolutions. The design of the adaptive parameter recovery protocol can be summarized in the following steps:

(1) By placing the initial probe state in the parameter channel and making it evolve, the density matrix  $\rho_g^{(n)}(T)$  at time  $T$  can be obtained for each  $g$ , where  $n$  indicates the  $n$ th batch with  $1 \leq n \leq N$ . Since  $g^* = 0.1$  corresponds to the real evolution of the system,  $\rho_{g^*}^{(n)}(T)$  represents the real density matrix of the system at time  $T$ . Thus, we can calculate the theoretical probabilities of four measurement outcomes  $\{m_0, m_1, m_2, m_3\}$  according to  $P^{*(n)}(m_l) = \text{Tr}[\rho_{g^*}^{(n)}(T)M_l^{(n)}]$ , where  $l \in \{0, 1, 2, 3\}$ .

(2) We obtain a sample set of  $R$  measurement outcomes of the  $n$ th batch by simulating the practical measurement process and sampling. Generally, according to the designed adaptive measurement scheme, one can apply the current measurement set to  $R$  independent evolutions to obtain a sample set of  $R$  measurement outcomes. While in the simulation, this can be conveniently realized by directly sampling  $R$  measurement outcomes according to the theoretical probability  $P^{*(n)}(m_l)$  of each measurement outcome. The obtained  $R$  measurement outcomes form a sample set of measurement outcomes of the  $n$ th batch, denoted as  $\vec{S}^{(n)}$ . Considering the possible projection measurement errors in practice, we discuss two scenarios: perfect sampling and imperfect sampling. The corresponding sets of samples are denoted by  $\vec{S}_p^{(n)}$  and  $\vec{S}_{np}^{(n)}$ , respectively. Perfect sampling implies that measurement outcomes are generated strictly according to the theoretical probabilities, and then  $\vec{S}_p^{(n)}$  is further obtained by randomly shuffling the order of the measurement outcomes.

Under imperfect sampling,  $\vec{S}_{np}^{(n)}$  is generated by using the roulette wheel method, where the cumulative probability of each measurement result is decided by

$$d_l^{(n)} = \sum_{i=0}^l P^{*(n)}(m_i), \quad l \in \{0, 1, 2, 3\}. \quad (31)$$

Concretely, a random number is first generated in  $(0, 1)$  by a computer. Then, the corresponding measurement outcome is

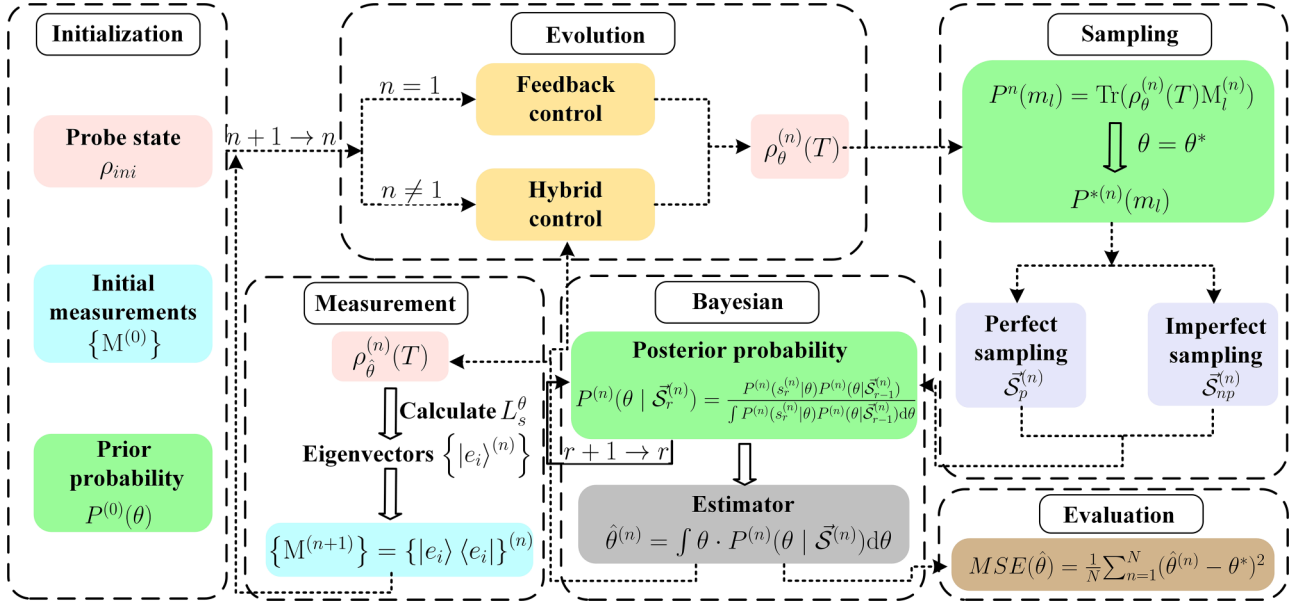


FIG. 9. The framework of the single-parameter quantum recovery protocol proposed in this paper, including initialization, evolution, sampling, Bayesian estimation, adaptive measurement, and evaluation steps.

determined by the interval it falls into. For example, if the random number falls into  $(0, d_0^{(n)})$ , then the measurement result is  $m_0$ ; if the random number is in  $(d_{l-1}^{(n)}, d_l^{(n)})$ , then the measurement result is  $m_l$ . This process is repeated  $R$  times to obtain a sample set of  $R$  measurement outcomes of the  $n$ th batch  $\tilde{S}_{np}^{(n)}$ .

(3) Based on the obtained sample set of measurement outcomes of the  $n$ th batch  $\tilde{S}^{(n)}$ , Bayesian estimation is used to update the probability distribution of  $g$ , i.e.,

$$P^{(n)}(g | \tilde{S}_r^{(n)}) = \frac{P^{(n)}(s_r^{(n)} | g) P^{(n)}(g | \tilde{S}_{r-1}^{(n)})}{\int P^{(n)}(s_r^{(n)} | g) P^{(n)}(g | \tilde{S}_{r-1}^{(n)}) dg}, \quad (32)$$

where  $s_r^{(n)}$  represents the  $r$ th element (measurement outcome) of the  $n$ th sample set  $\tilde{S}^{(n)}$  with  $1 \leq r \leq R$ , and  $\tilde{S}_r^{(n)}$  represents the set of the first  $r$  elements of  $\tilde{S}^{(n)}$ . For each element  $s_r^{(n)}$ , the posterior probability of  $s_r^{(n)}$  acts as the prior probability of  $s_{r-1}^{(n)}$ , and then the new posterior probability of  $s_r^{(n)}$  is calculated via Eq. (32). After all the elements of  $\tilde{S}^{(n)}$  are used to update Eq. (32) in turn, the final probability distribution of  $g$  for the  $n$ th batch can be obtained. Based on the obtained probability distribution, a new estimate can be yielded by utilizing the Bayesian estimator  $\hat{g}^{(n)} = \int g P^{(n)}(g | \tilde{S}^{(n)}) dg$ . Meanwhile, the POVM for the next batch is updated according to the new estimate, as described in Sec. IV A. With the new POVM, a new batch is started from Step 1 until the maximum batch  $N$ .

(4) After obtaining the estimates of  $g$  for all batches, we choose an evaluation indicator to measure the estimation performance. Here, the parameter recovery result is evaluated by using the mean square error (MSE), i.e.,

$$MSE(\hat{g}) = \frac{1}{N} \sum_{n=1}^N (\hat{g}^{(n)} - g^*)^2, \quad (33)$$

where  $\hat{g}^{(n)}$  represents the estimate of the  $n$ th batch.

In view of the factors such as experiment overhead, time cost, and limited prior knowledge, the final estimation precision of the protocol is difficult to reach the quantum precision limit. However, it has the advantages of simplicity, efficiency, and practicality in implementation. In the next subsection, we will integrate the two control strategies proposed in Sec. III into the parameter recovery protocol and analyze the recovery performance.

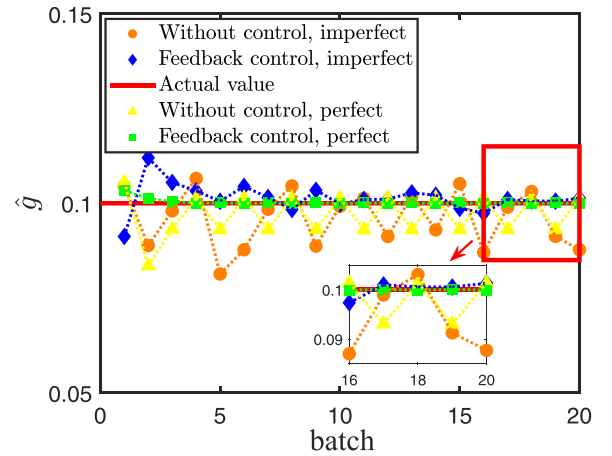


FIG. 10. Estimates of  $\hat{g}$  in the ZZ-coupled systems with respect to iterative batches (with or without feedback control) at different sample levels, where an enlarged view indicates the results of batches 16–20. The solid red line represents the true value of  $g$ , i.e.,  $g^* = 0.1$ . The orange circles and yellow triangles represent the estimation results without control under imperfect sampling and perfect sampling, respectively. The blue diamonds and green squares are the estimation results with feedback control under imperfect sampling and perfect sampling, respectively. Other parameters are chosen as  $\omega_1 = \omega_2 = 1$  and  $\gamma = 0.05$ .

TABLE I. Mean square errors of parameter estimation under different values of  $g^*$ .

	Control strategy	Imperfect sampling	Perfect sampling
$g^* = 0.05$	Without control	$1.59 \times 10^{-4}$	$7.89 \times 10^{-5}$
	Feedback control	$5.13 \times 10^{-5}$	$3.74 \times 10^{-5}$
	Hybrid control	$2.62 \times 10^{-5}$	$9.30 \times 10^{-6}$
$g^* = 0.1$	Without control	$7.04 \times 10^{-5}$	$3.97 \times 10^{-5}$
	Feedback control	$3.67 \times 10^{-5}$	$1.75 \times 10^{-5}$
	Hybrid control	$1.79 \times 10^{-5}$	$5.47 \times 10^{-6}$
$g^* = 0.15$	Without control	$1.16 \times 10^{-4}$	$6.92 \times 10^{-5}$
	Feedback control	$4.68 \times 10^{-5}$	$3.15 \times 10^{-5}$
	Hybrid control	$3.09 \times 10^{-5}$	$7.22 \times 10^{-6}$

### C. Performance analysis

First, we discuss the effect of feedback control in the parameter recovery protocol. The feedback operator is still chosen as  $U_{fb} = e^{i\frac{\pi}{2}\sigma_x} \otimes I$ . Perfect sampling and imperfect sampling are used to simulate the system without and with feedback control. The estimates of  $g$  are shown in Fig. 10. It can be seen that under free evolution, the estimated values exhibit significant fluctuations around the true value. The enlarged graph more intuitively shows that there is no decreasing trend in fluctuations without control. In contrast, the estimates under feedback control, whether with perfect or imperfect sampling, show a better convergence trend. In the case of perfect samples, the estimated values closely match the true value in early iterations. Such an improvement trend in estimation precision is consistent with that under the feedback control scheme in Sec. III.

Next, we discuss the effect of hybrid control in the parameter recovery protocol. Since additional Hamiltonian control is based on optimization and thereby easily leads to local optimum in the absence of prior knowledge, we can apply only feedback control to the first batch ( $n = 1$ ) to acquire some parameter information. Upon entering the second batch ( $n = 2$ ), the hybrid scheme is launched. The GRAPE algorithm is utilized to obtain an optimal control  $\vec{u}^{(k)}$  ( $k = 1, 2$ ), which acts on the system as the Hamiltonian control together with feedback control. This process iterates sequentially until the maximum batch  $N$  is reached. Finally, the MSEs under different scenarios are presented in Table I, where we use the measurement operators in Eq. (30) as initial measurements. It can be seen that under the same control strategy, perfect sampling exhibits lower errors compared to imperfect sampling. In the three scenarios with different values of  $g^*$ , compared with free evolution, the two control strategies proposed in this paper significantly reduce the MSEs of estimation. This validates the effectiveness of combining adaptive measurement with control strategies, making the entire quantum parameter recovery protocol easier to implement and more efficient. It should be emphasized that MSEs in Table I achieve satis-

factory estimation accuracies in all cases, although the initial measurement operators in Eq. (30) may be not optimal for the parameter values of  $g^* = 0.05$  and  $g^* = 0.15$ . This is because the adaptive update of the measurement operators plays a good role.

### V. CONCLUSION

In this paper, we have presented a complete process of quantum parameter estimation for a ZZ-coupled system. To improve the estimation precision of the coupling coefficient  $g$ , two control strategies including feedback control and hybrid control were proposed. In the feedback control strategy, we have found a stable feedback operator that acts on only one qubit and can significantly improve estimation performance. In the hybrid control strategy, by combining feedback control with additional Hamiltonian control, the estimation precision was further improved. Compared with free evolution, both control strategies exhibit superior estimation performance and significantly slow down the rate of decoherence. On the other hand, to enhance the connection between theory and practice, a practical quantum parameter recovery protocol based on Bayesian estimation theory has been proposed. This protocol combines batch adaptive measurement with two aforementioned control strategies. The parameter recovery results verify the effectiveness of the two schemes in improving estimation precision. We point out that the protocol proposed in this paper is also applicable to the improvement of other quantum performances, such as stable entropy squeezing in atomic systems.

In future research, the problem of multiparameter estimation of quantum systems will be explored using similar hybrid control and adaptive measurement schemes. Although there have been many studies on multiparameter estimation in quantum systems [25,34], there still exist some challenges, e.g., how to select the optimal measurement set to achieve the simultaneous high-precision estimation of multiparameters such as the dissipation rate  $\gamma$  and local frequency  $\omega$  under different prior knowledge, and how to consider limitations on control resources from an experimental perspective. We expect to extend the schemes proposed in this paper to multiparameter scenarios to better address these issues. In addition, under higher requirements for estimation accuracy, practical single- or multiparameter recovery protocols are worth further investigating, which involve the optimization and improvement of measurement schemes and estimation protocols.

### ACKNOWLEDGMENTS

The work is partially supported by the National Natural Science Foundation of China under Grant No. 62373342 and the Australian Research Council's Future Fellowship funding scheme under Project No. FT220100656.

- [1] V. Giovannetti, S. Lloyd, and L. Maccone, Advances in quantum metrology, *Nat. Photon.* **5**, 222 (2011).  
 [2] J. Liu, M. Zhang, H. Chen, L. Wang, and H. Yuan, Optimal scheme for quantum metrology, *Adv. Quantum Technol.* **5**, 2100080 (2022).

- [3] S. Pang and T. A. Brun, Quantum metrology for a general Hamiltonian parameter, *Phys. Rev. A* **90**, 022117 (2014).  
 [4] S. Kimmel, G. H. Low, and T. J. Yoder, Robust calibration of a universal single-qubit gate set via robust phase estimation, *Phys. Rev. A* **92**, 062315 (2015).

- [5] L. Gyongyosi, Unsupervised quantum gate control for gate-model quantum computers, *Sci. Rep.* **10**, 10701 (2020).
- [6] Z. Ji, G. Wang, R. Duan, Y. Feng, and M. Ying, Parameter estimation of quantum channels, *IEEE Trans. Inf. Theory* **54**, 5172 (2008).
- [7] C. Lupo, C. Ottaviani, P. Papanastasiou, and S. Pirandola, Parameter estimation with almost no public communication for continuous-variable quantum key distribution, *Phys. Rev. Lett.* **120**, 220505 (2018).
- [8] Q. Tan, W. Wu, L. Xu, J. Liu, and L. Kuang, Quantum sensing of supersensitivity for the Ohmic quantum reservoir, *Phys. Rev. A* **106**, 032602 (2022).
- [9] C. Bonato, M. S. Blok, H. T. Dinani, D. W. Berry, M. L. Markham, D. J. Twitchen, and R. Hanson, Optimized quantum sensing with a single electron spin using real-time adaptive measurements, *Nat. Nanotechnol.* **11**, 247 (2016).
- [10] Y. Chu, S. Zhang, B. Yu, and J. Cai, Dynamic framework for criticality-enhanced quantum sensing, *Phys. Rev. Lett.* **126**, 010502 (2021).
- [11] L. Liu and H. Yuan, Achieving higher precision in quantum parameter estimation with feedback controls, *Phys. Rev. A* **102**, 012208 (2020).
- [12] H. Hong, T. Huang, X. Lu, and S. Kuang, Enhancing the precision of multi-parameter estimation for two-level open quantum system by mixed control, *Quantum Inf. Process.* **21**, 240 (2022).
- [13] Q. Zheng, L. Ge, Y. Yao, and Q. Zhi, Enhancing parameter precision of optimal quantum estimation by direct quantum feedback, *Phys. Rev. A* **91**, 033805 (2015).
- [14] J. Liu and H. Yuan, Quantum parameter estimation with optimal control, *Phys. Rev. A* **96**, 012117 (2017).
- [15] J. Zhao, D. Chen, Y. Zhang, Y. Fang, M. Yang, Q. Wu, and C. Yang, Coherence and quantum Fisher information in general single-qubit parameter estimation processes, *Phys. Rev. A* **104**, 062608 (2021).
- [16] P. Sekatski, M. Skotiniotis, and W. Dür, Improved sensing with a single qubit, *Phys. Rev. Lett.* **118**, 170801 (2017).
- [17] L. T. Kenfack, W. D. W. Gueagni, M. Tchoffo, and L. C. Fai, Quantum thermometry by single qubit-probe in a thermal XY spin-chain bath, *Quantum Inf. Process.* **20**, 144 (2021).
- [18] C. Gonzalez-Ballester, E. Moreno, and F. J. Garcia-Vidal, Generation, manipulation, and detection of two-qubit entanglement in waveguide QED, *Phys. Rev. A* **89**, 042328 (2014).
- [19] M. E. Kimchi-Schwartz, L. Martin, E. Flurin, C. Aron, M. Kulkarni, H. E. Tureci, and I. Siddiqi, Stabilizing entanglement via symmetry-selective bath engineering in superconducting qubits, *Phys. Rev. Lett.* **116**, 240503 (2016).
- [20] F. Tacchino, A. Chiesa, S. Carretta, and D. Gerace, Quantum computers as universal quantum simulators: state-of-the-art and perspectives, *Adv. Quantum Technol.* **3**, 1900052 (2020).
- [21] S. Qin, M. Cramer, C. Koch, and A. Serafini, Optimal control for Hamiltonian parameter estimation in non-commuting and bipartite quantum dynamics, *SciPost Phys.* **13**, 121 (2022).
- [22] J. Liu and H. Yuan, Control-enhanced multiparameter quantum estimation, *Phys. Rev. A* **96**, 042114 (2017).
- [23] Z. Hou, R. Wang, J. Tang, H. Yuan, G. Xiang, C. Li, and G. Guo, Control-enhanced sequential scheme for general quantum parameter estimation at the Heisenberg limit, *Phys. Rev. Lett.* **123**, 040501 (2019).
- [24] L. Bao, B. Qi, Y. Wang, D. Dong, and R. Wu, Multi-channel quantum parameter estimation, *Sci. China Inf. Sci.* **65**, 200505 (2022).
- [25] M. Zhang, H. Yu, H. Yuan, X. Wang, R. Demkowicz-Dobrzański, and J. Liu, QuanEstimation: An open-source toolkit for quantum parameter estimation, *Phys. Rev. Res.* **4**, 043057 (2022).
- [26] H. Xu, L. Wang, H. Yuan, and X. Wang, Generalizable control for multiparameter quantum metrology, *Phys. Rev. A* **103**, 042615 (2021).
- [27] H. Xu, J. Li, L. Liu, Y. Wang, H. Yuan, and X. Wang, Generalizable control for quantum parameter estimation through reinforcement learning, *npj Quantum Inf.* **5**, 82 (2019).
- [28] H. Hong, X. Lu, and S. Kuang, Feedback control and quantum error correction assisted quantum multi-parameter estimation, *Chin. Phys. B* **32**, 040603 (2023).
- [29] D. Dong and I. R. Petersen, Quantum estimation, control and learning: Opportunities and challenges, *Annu. Rev. Control* **54**, 243 (2022).
- [30] A. R. R. Carvalho and J. J. Hope, Stabilizing entanglement by quantum-jump-based feedback, *Phys. Rev. A* **76**, 010301(R) (2007).
- [31] R.-Y. Wu and M.-F. Fang, Controlling the entropic uncertainty and quantum discord in two two-level systems by an ancilla in dissipative environments, *Chin. Phys. B* **30**, 037302(R) (2021).
- [32] Y. Li, B. Luo, and H. Guo, Entanglement and quantum discord dynamics of two atoms under practical feedback control, *Phys. Rev. A* **84**, 012316 (2011).
- [33] H. T. Dinani, D. W. Berry, R. Gonzalez, J. R. Maze, and C. Bonato, Bayesian estimation for quantum sensing in the absence of single-shot detection, *Phys. Rev. B* **99**, 125413 (2019).
- [34] K. K. Lee, C. N. Gagatsos, S. Guha, and A. Ashok, Quantum-inspired multi-parameter adaptive Bayesian estimation for sensing and imaging, *IEEE J. Sel. Top. Signal Process.* **17**, 491 (2023).
- [35] Y. Ma, M. Pang, L. Chen, and W. Yang, Improving quantum parameter estimation by monitoring quantum trajectories, *Phys. Rev. A* **99**, 032347 (2019).
- [36] C. Shao and H. Xiang, Quantum regularized least squares solver with parameter estimate, *Quantum Inf. Process.* **19**, 113 (2020).
- [37] Y. Wang, S. Yokoyama, D. Dong, I. R. Petersen, E. H. Huntington, and H. Yonezawa, Two-stage estimation for quantum detector tomography: Error analysis, numerical and experimental results, *IEEE Trans. Inf. Theory* **67**, 2293 (2021).
- [38] K. Rambhatla, S. E. D'Aurelio, M. Valeri, E. Polino, N. Spagnolo, and F. Sciarrino, Adaptive phase estimation through a genetic algorithm, *Phys. Rev. Res.* **2**, 033078 (2020).
- [39] I. Kull, P. A. Guérin, and F. Verstraete, Uncertainty and trade-offs in quantum multiparameter estimation, *J. Phys. A: Math. Theor.* **53**, 244001 (2020).
- [40] J. Liu, H. Yuan, X. Lu, and X. Wang, Quantum Fisher information matrix and multiparameter estimation, *J. Phys. A: Math. Theor.* **53**, 023001 (2020).
- [41] J. Liu, J. Chen, X. X. Jing, and X. G. Wang, Quantum Fisher information and symmetric logarithmic derivative via anti-commutators, *J. Phys. A: Math. Theor.* **49**, 275302 (2016).
- [42] H. M. Wiseman, Quantum theory of continuous feedback, *Phys. Rev. A* **49**, 2133 (1994).